Highly selective zinc ion removal by the synergism of functional groups and defects from N, S co-doped biochar

Changlin Wang [a], Santosh Adhikari [b], Yuqi Li [a], Mingjian Wen [b], Yang Wang [a,c,d,*]

[a] School of Chemical Engineering and Technology, Tianjin University, Tianjin 300350, China
[b] Chemical and Biomolecular Engineering, University of Houston, Houston 77204, TX, USA
[c] Tianjin Key Laboratory of Membrane Science and Desalination Technology, Tianjin 300072, China
[d] National Industry-Education Integration Platform of Energy Storage, Tianjin University, Tianjin 300350, China

ARTICLE INFO

ABSTRACT

Capacitive deionization (CDI) is a promising technology for selectively removing Zn^{2+} ions from industrial wastewater that contains a wide variety of ions. A key task in implementing effective CDI systems lies in the selection and optimization of electrode materials. In this work, a hierarchical porous biochar from the chestnut inner shell was developed by N, S element doping, providing a large ion-accessible surface area with abundant functional groups and defects. The increased defect sites (defect ratio of 1.09) and specific surface area (2029.1 $m^2\ g^{-1}$) provided substantial sites for Zn^{2+} adsorption, and the specific functional groups endowed high Zn^{2+} selectivity. The N, S co-doped biochar achieved a Zn^{2+} adsorption of 706.4 μmol g^{-1} at 1.0 V and a selectivity factor of 14.9 against Na^+. Importantly, the defects created by N doping enhanced the ion adsorption capacity, and N, S functional groups strengthened the selectivity of Zn^{2+} adsorption, which were elucidated by in situ Raman spectroscopy and further validated by density functional theory (DFT) calculations. The N, S co-doped biochar with high adsorption capacity and excellent selectivity provides a novel insight for the treatment of wastewater with low Zn^{2+} concentration and further advances the practical application of CDI technology.

1. Introduction

Global industrialization has led to a surge in wastewater disposal, and a diverse kind of heavy metal ions have been released into the natural environment [1]. Zinc, a highly versatile metal, is widely applied in the production of various industrial products, such as zinc-coated metal [2], lacquer [3], cosmetics [4], and Zn ion batteries, generating large quantities of Zn-containing wastewater. Zn^{2+} poses a severe threat to environmental safety and public health due to its toxic and non-biodegradable nature [5]. Once the Zn^{2+} concentration in water exceeds the regulated level, it can trigger problems in many human systems [6]; it also affects plant growth [7] and exposes aquatic microorganisms and marine life to danger [8]. As a result, World Health Organization (WHO) has identified zinc as a toxic and hazardous metal, and Zn-containing wastewater should be released at a concentration below 5 ppm [9]. On the other hand, as mentioned above, zinc is a crucial metal in numerous industrial applications, making its recovery from wastewater highly valuable. By utilizing technical means to recover Zn^{2+}, we can protect the environment and promote the sustainable use of resources through recycling.

Various approaches have been utilized for the removal or recycling of Zn^{2+} from industrial wastewater, such as biomass adsorption [10], coagulation flocculation or chemical precipitation [11], electrodialysis [12] and ion-exchange membranes [13]. However, the capacity of physical adsorption is poor, chemical precipitation consumes a considerable amount of reagents and is prone to secondary pollution, electrodialysis and ion exchange membranes are highly efficient but require a tremendous amount of energy and a substantial cost [14,15]. Consequently, it is crucial to explore alternative technology for Zn^{2+} removal with superior separation performance and low cost. Capacitive deionization (CDI) is considered a promising technology for wastewater treatment [16]. In CDI, an electrical potential difference is applied between two electrodes, which attracts charged ions from the aqueous solution to the electrode surfaces, effectively removing them from the wastewater [17,18]. CDI is relatively simple to operate and does not introduce secondary pollution, and it has been employed for a couple of heavy metal ions [19].

The treatment of Zn-containing wastewater is a challenging task,

---

* Corresponding author at: School of Chemical Engineering and Technology, Tianjin University, Tianjin 300350, China.
E-mail address: yangwang2017@tju.edu.cn (Y. Wang).

especially for low Zn^{2+} concentration of less than 100 ppm. In industrial wastewater, Zn^{2+} often exists alongside other ions such as Na^+, Cr^{3+}, and Ni^{2+}, and thus a key issue lies in designing electrodes that are highly selective for Zn^{2+}. Biochar is derived from the pyrolysis of biomass, which is widely produced from agriculture and industry as cost-effective and renewable waste. The relatively inexpensive price and environmentally friendly attributes, coupled with its ease of modification, have made it a popular choice in CDI. The capacity and selectivity of biochar can be further exemplified by compositing with metal oxide, heteroatom doping, and other modifications. Gaikwad et al. [20] achieved a Cr (VI) adsorption of 2.8 mg g^{-1} at 1.2 V by treating rice husk-based activated carbon with acid. Wang et al. [21] coupled Fe_3O_4 onto waste oil tea shell-based activated carbon and enhanced the removal of Cd^{2+}, achieving an adsorption capacity of 34.22 mg g^{-1} at 1.2 V. Huang et al. [22] prepared an N, P co-doped Sargassum biochar using microwaves and demonstrated 67.09 mg g^{-1} of Cu^{2+} removal at 1.2 V. These achievements show that the optimization of biochar is an effective approach to attain selective ion removal.

Chestnuts are widely cultivated in Europe and Asia, and chestnut inner shell-based biochar can form a distinctive layered structure due to the unique linkage. Previous investigations on the chestnut inner shell-based biochar have shown excellent desalination performance [23–25]. Herein, we have developed an N, S co-doped hierarchical porous carbon with a large ion-accessible surface area, using chestnut inner shells as the carbon source. During the carbonization process, N atoms can be doped into the carbon skeleton, altering the intrinsic structure and introducing more defective sites, which can enhance the adsorption capacity for Zn^{2+}. Pyridine N was introduced to realize the selective adsorption of Zn^{2+}. S atoms can be anchored into the pores as —SO_3H by interfacial engineering to optimize the hydrophilicity and promote the adsorption of Zn^{2+}. The electrode was characterized with various advanced techniques, showing the structural (defect sites) and surface (functional groups) features of the biochar. The electrochemical performance and selective adsorption capacity were investigated with several electrochemical methods and desalination experiments in mixed solutions. We obtained a high Zn^{2+} adsorption of 706.4 µmol g^{-1} at 1.0 V and a selectivity factor of 14.9 against Na^+. In addition, the synergistic mechanism of defect sites and functional groups on the desalination performance was further revealed by in situ Raman and DFT. This work provides a novel approach for the efficient removal of Zn^{2+} in solutions containing low concentrations of Zn^{2+}.

2. Materials and methods

2.1. N, S co-doped biochar and electrode fabrication

The chestnut inner shell was supplied from a farm in Henan Province, China, without further treatment. HCl and dicyandiamide were obtained from Shanghai Macklin Biochemical Co., Ltd. KOH, anhydrous ethanol, and hexane were supplied from Tianjin Yuanli Chemical Co., Ltd. H_2SO_4 was purchased from Rianlong Co., Ltd. polyvinylidene difluoride (PVDF) and carbon black were purchased from Arkema Kynar and Cabot, respectively. The N-methyl-2-pyrrolidone (NMP) was purchased from Tianjin Fuchen Chemical Co., Ltd. All reagents were of analytical grade and used without purification.

A schematic overview of the material preparation procedure is presented in Fig. 1. 10 g chestnut inner shell was mixed with dicyandiamide in the mass ratio of 1:2 in a solution of 200 mL of deionized water and 200 mL of anhydrous ethanol. The mixture was mechanically stirred for 4 h and then dried. The dried powder was heated up to 600 °C at a rate of 4 °C min^{-1} under an N_2 atmosphere and maintained for 2 h in a tube furnace. Subsequently, 2 g of carbonized chestnut inner shell and 6 g of KOH were mixed in 8 mL of deionized water, and the suspension was stirred for 2 h and ultrasonicated for 2 h before dried at 60 °C for 12 h. Next, the product was heated to 800 °C under N_2 atmosphere at the same rate for 1 h. The excessive KOH and impurities were washed with 0.5 M HCl, and then with deionized water until the pH was 7. After drying, the biochar was ground and passed through a 200-mesh sieve. 1 g of powder was immersed in 7 mL of H_2SO_4 (20 wt%) for 24 h. Later, it was immersed in excessive hexane for 10 min to allow the H_2SO_4 to sink and separate. The powder was immersed in 500 mL of ice water for 30 min, then in 200 mL of deionized water for 30 min, and repeated three times. The final powder was dried at 60 °C overnight and designated as NSBc. All the mechanical mixing speeds were set at 400 rpm unless noted. The preparation method of pristine biochar (PBc) can be found in our previous research [25].

The obtained samples (PBc, NSBc) were mixed with carbon black, and fully ground in the mortar to make it evenly mixed. Subsequently, it was dispersed in a 32 mg mL^{-1} PVDF slurry in NMP. The mass ratio of biochar, carbon black, and PVDF was 8: 1: 1. The mixed slurry was prepared by magnetic stirring for 24 h and then coated on a graphite plate with a doctor blade (200 µm). The area of the active material was 2 × 2 cm and 4 × 5 cm for electrochemical tests and desalination experiments, respectively. The electrodes were then dried at 60 °C for 12 h.

2.2. Materials characterizations

The morphology of the prepared materials was observed via scanning electron microscopy (SEM, Regulus 8100) and transmission electron microscope (TEM, JEM-F200). The element mapping was obtained by energy dispersive spectroscopy (TEM-EDS). Nitrogen adsorption–desorption isotherms were collected at 77 K (Autosorb IQ3, Quantachrome) and calculated by the Brunauer-Emmett-Teller (BET) method to obtain the specific surface area and pore size distribution. The crystal structure was characterized by X-ray diffraction (XRD, D8 Focus, Bruker). Functional groups were obtained using Fourier transfer infrared spectroscopy (FT-IR, Nicolet iS5) with KBr in the range of 400–4000 cm^{-1}. Hydrophilicity was measured by a water contact angle test instrument (CA100D). Raman spectra were obtained on LabRAM HR Evolution (HORIBA) with a laser wavelength of 532 nm. X-ray photoelectron spectroscopy (XPS) using Al K Alpha was performed on ESCA-LAB 250Xi to measure the chemical bonds and functional groups of materials. The concentration of various ions in a mixed solution was detected by the inductively coupled plasma-optical emission spectrometry (ICP-OES, Agilent 5110).

A self-designed PMMA electrochemical cell was used for in situ Raman measurement. The potential was applied by a Gamry electrochemical workstation. Raman spectra were recorded by LabRAM HR
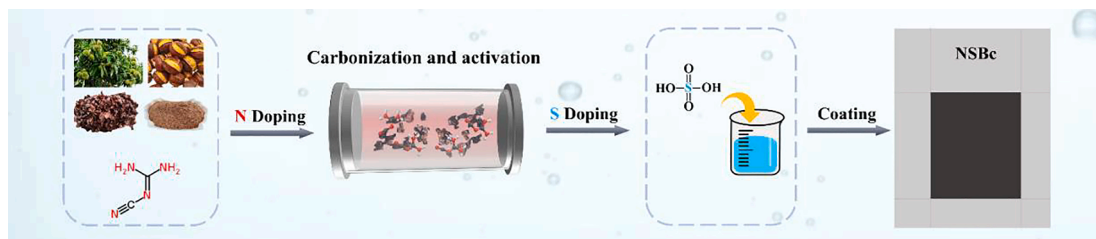

Fig. 1. Schematic of N, S co-doped biochar synthesis.

Evolution Raman spectrometer and the excitation light source of the laser was 532 nm utilizing a single grating mode (600 lines). Focusing with a 50-fold long focal lens, the surface of the working electrode is vertically illuminated. A two-electrode system was utilized for the test and the size of the electrodes was 4 × 5 cm. The applied voltage was 1.0 V for 50 min and the data was recorded at 10-minute intervals.

2.3. Electrochemical tests

The electrochemical measurements were performed in 0.5 M NaCl or ZnCl$_2$ solution using an electrochemical workstation (Biologic VSP300). A typical three-electrode system was employed, consisting of a 2 × 2 cm working electrode, a saturated calomel electrode (SCE) as the reference electrode, and a 3 × 3 cm platinum mesh as the counter electrode. Cyclic voltammetry (CV) experiments were conducted under different scanning rates from 5 to 50 mV s^{-1} within −1.0 to 0 V. The specific capacitance (C_{sv}, F g^{-1}) of the electrode was obtained by Eq. (1):

$$C_{sv} = \frac{\int I \mathrm{d}v}{2vm\Delta V} \tag{1}$$

where I stand for the current, v is the scan rate, m represents the mass loading of the electrode, and ΔV corresponds to the potential range.

The electrode was also evaluated by the galvanostatic charge/discharge (GCD) method, varying the current density of 0.2 to 1.4 A g^{-1} within −0.6 to 0 V. The specific capacitance C_s were calculated from the discharge curves by Eq. (2):

$$C_s = \frac{i\Delta t}{m\Delta V} \tag{2}$$

where i stands for the current density, Δt is the discharging time, m represents the mass loading of the electrode, and ΔV corresponds to the potential range.

Electrochemical impedance spectroscopy (EIS) was performed at frequencies ranging from 10 mHz to 100 kHz, applying an alternating current amplitude of 10 mV around the open circuit potential. The potential of zero charge (Epzc) was obtained by the CV method under the scan rate of 1 mV s^{-1} within −0.5 to 0.5 V. in a 5 mM single NaCl or ZnCl$_2$ solution.

2.4. CDI experiments

CDI experiments were performed using batch mode under constant voltage. The voltage for the adsorption process was 1.0 V for 100 min, and the desorption process was 0 V for 100 min. The total mass loading of the anode and cathode is about 30 mg. 60 mL of feed water was circulated at a flow rate of 30 mL min^{-1}, with the flow rate being controlled by a peristaltic pump (Shenchen Precision Pump Co., Ltd.), between the 3D-printed tank and the reactor. The feed water was 1 mM NaCl, 1 mM ZnCl$_2$, or a mixed solution containing 1 mM ZnCl$_2$ and x mM NaCl (x = 1, 3). The different electrode configurations (labeled as PBc//PBc, NSBc//NSBc) were investigated and compared. The salt adsorption capacity (SAC, μmol g^{-1}) and the average salt adsorption rates (ASAR, μmol g^{-1} min^{-1}) were defined by Eq. (3) and Eq. (4), respectively:

$$SAC = \frac{(C_o - C_e)V}{m} \tag{3}$$

$$ASAR = \frac{SAC}{t} \tag{4}$$

where the C_o and C_e are the initial and final concentrations of salt solution, respectively, V is the volume of solution, and m is the total mass of the two electrodes.

To elucidate the capacity of the electrode to remove Zn^{2+} in the condition containing Na$^+$, a selectivity coefficient (Zn^{2+}/Na$^+$) was introduced, which was calculated by Eq. (5):

$$\beta\left(\frac{Zn^{2+}}{Na^+}\right) = \frac{Q_{Zn^{2+}}}{Q_{Na^+}} / \frac{C_{Zn^{2+}}}{C_{Na^+}} \tag{5}$$

where the Q_{Zn}^{2+} and Q_{Na}^+ (μmol g^{-1}) are adsorption capacity of NSBc for Zn^{2+} and Na$^+$, respectively. C_{Zn}^{2+} and C_{Na}^+ are denoted as the initial concentrations of ions.

2.5. Density functional theory calculations

We performed density functional theory (DFT) calculations using the Vienna Ab initio Simulation Package (VASP) [26,27] version 6.4.2 with periodic boundary conditions. Standard projector augmented wave (PAW) pseudopotentials [28,29] were employed for all elements. The Perdew-Burke-Ernzerhof (PBE) functional [30] was adopted and the many-body dispersion (MBD) method [31] was added to account for van der Waals (vdW) interactions. All calculations were conducted under spin-polarized conditions, and structures were optimized to achieve convergence within 10^{-6} eV. We expedited these relaxation procedures using Gaussian smearing with a width of 0.02 eV. Throughout our computations, a plane-wave cutoff of 520 eV was maintained. For all calculations, Γ centered 4 × 4 × 1 k-mesh were used to sample the Brillouin zone.

Recent studies suggest that the adsorption energy (E_{ads}) obtained from conventional gas-phase calculations is significantly altered by the presence of the solvents [32,33]. This indicates that the polarization effects, the solvents introduce, are critical for accurately describing adsorption energies. To evaluate the impact of an implicit solvent, we employed the VASsol module [34,35]. These calculations were carried out as single-point calculations on DFT-optimized (gas-phase) geometries. Default settings for cavitation energy were utilized, and the plane-wave energy cutoff was raised to 800 eV to ensure accurate results. We calculated E_{ads} by subtracting the energy of the Slab + Molecule system from that of the slab and the isolated molecule, as shown in Eq. (6), all in the presence of an implicit solvent (water).

$$E_{ads} = E_{Slab} + E_{Molecule} - E_{Slab+Molecule}. \tag{6}$$

3. Results and discussion

3.1. Materials characterization

The morphological structure of the prepared samples was characterized by SEM and TEM as shown in Fig. 2. The SEM image (Fig. 2a–c) of PBc shows that the unmodified biochar possesses lots of macropores on the surface. In Fig. 2d–f, NSBc exhibits an irregular sponge-like shape, which is covered with porous structures of different sizes. The morphology of NSBc was drastically changed after doping. These structures are interwoven and provide abundant pores for ion adsorption [36]. Furthermore, NSBc contains plenty of micropores and mesopores observed by TEM (Fig. 2g and h), which can effectively enhance the ion adsorption capacity. Moreover, a limited amount of fragmented graphite structure can be observed, which is conducive to electron transfer [37]. The results of the elemental mapping are presented in Fig. 2i, where the N and S atoms were successfully doped onto the biochar and uniformly distributed on the surface. The amount of N was higher than S due to the different doping routes and dosages.

Nitrogen adsorption/desorption was used to analyze the pore structure of the material, and the results are presented in Fig. 3a. According to the IUPAC classification, PBc shows typical type I adsorption curves and NSBc exhibits the type IV isotherm with an H4 hysteresis loop [38]. It is clear that PBc is dominated by micropores while both micropores and mesopores can be observed in NSBc, which also agrees with the SEM and TEM results. Furthermore, the pore size distribution is depicted in Fig. 3b, and there are a certain number of mesopores with a size of 3–10 nm in NSBc, which can provide enough buffer channels for ion adsorption [39]. The BET surface area of NSBc is 2029.1 m^2 g^{-1},
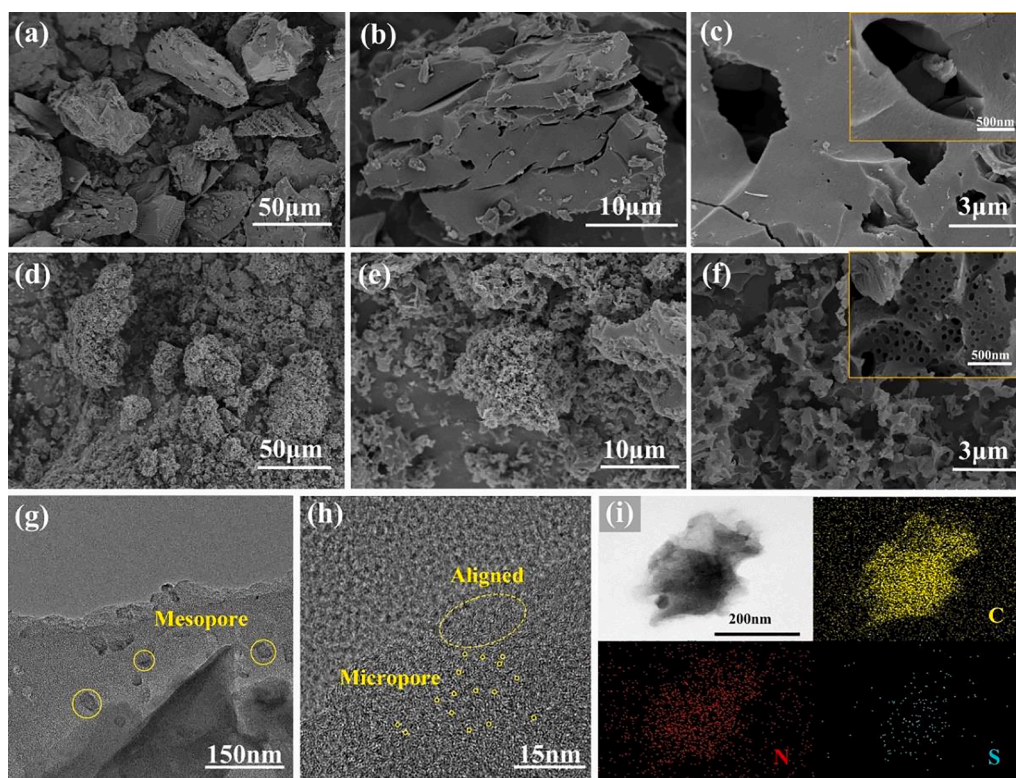
Fig. 2. SEM images of (a-c) PBc and (d-f) NSBc; TEM images (g, h) and elemental mapping (i) of NSBc.

which is larger than that of PBc (1693.8 m^2 g^{-1}). Obviously, the introduction of N atoms in the synthetic process significantly changes the porosity and microstructures of the biochar with a larger specific surface area and total pore volume, which are supposed to facilitate the charge storage capacity and desalination performance [40].

XRD was carried out to analyze the crystal structures. As shown in Fig. 3c, two broad peaks appear at 22° and 43°, corresponding to the (0 0 2) and (1 0 0) diffraction modes of the graphite structure, which are typical of disordered carbon [41]. Compared with PBc, it indicates that N, S doping does not affect the crystal structure of biochar.

The FTIR spectra of PBc and NSBc were carried out and presented in Fig. 3d. The peaks observed at 3434 cm^{-1} can be attributed to the O—H/N—H stretching vibration, while the peaks at 2920 cm^{-1} and 2855 cm^{-1} are ascribed to the C—H stretching vibration mode [42]. Furthermore, the peaks observed at 1587/1591 cm^{-1} can be attributed to the C—N stretching vibration mode of benzoid rings in pyridine N and pyrazine N. The presence of this peak in both samples is owing to the fact that the chestnut inner shell itself contains a certain amount of N. Additionally, a minor peak attributable to C≡N is discernible at 2099 cm^{-1} in NSBc. It is evident that at 1093 cm^{-1}, NSBc manifests a more pronounced peak than PBc. This increase come from the symmetric and asymmetric stretching vibrations of O=S=O in the S-group functional group, in conjunction with the C—O and C—O—C bonds of biochar [43]. Moreover, an S—O bond vibration peak is observed at 958 cm^{-1} for NSBc. These results demonstrate the efficacy of the N and S elements doping process.

Raman spectroscopy was employed to depict the defects created by the element doping. In Fig. 3e, D and G bands can be observed at 1335 cm^{-1} and 1589 cm^{-1}, which is related to defects induced A_{1g} vibration mode of sp^3 carbon rings and E_{2g} vibration mode of sp^2 carbon atom [44]. The defects can be categorized into carbon intrinsic defects and external defects caused by the doping of N atoms. By calculating the peak intensity ratio of the D band and G band, the value of NSBc is 1.09 higher than that of PBc (1.01). Notably, the strength of the G band hardly changes and the main change is from the D band, indicating that NSBc produces more defects owing to the introduction of N atoms without affecting the graphitization of the material largely. The N, S atoms doping leads to the formation of defective sites with lone pairs of electrons in the graphite crystalline layer, and these lone pairs of electrons can promote electron transport in the carbon matrix and increase the ion concentration in the double layer, thereby improving the double layer capacitance and increasing the ion storage capacity [45].

To further investigate the hydrophilic property of materials, the contact angle analyses are shown in Fig. 3f. It can be observed that NSBc possesses a smaller water contact angle compared to PBc, indicating that the hydrophilicity of NSBc is superior, which is attributed to the formation of abundant functional groups from the N atoms doping in the skeleton as well as the S atoms doping on the surface. The decreased surface free energy is predicted to promote the ion transport process at the solid–liquid interface and improve the desalination performance [46].

3.2. Electrochemical performance

The CV curves of PBc, and NSBc in various solutions at 5 mV s^{-1} in the potential range of $-1.0 - 0$ V are shown in Fig. 4a. PBc exhibits the quasi-rectangular like shape in NaCl solution, indicating the pure capacitive performance of the Na^+ adsorption, while it presents a relatively distorted shape in $ZnCl_2$ solution, suggesting that the capacitive adsorption of Zn^{2+} is accompanied by slightly pseudocapacitive adsorption. It is noteworthy that NSBc exhibits a greater degree of distortion compared to PBc owing to the pyridine N and —SO$_3$H producing more pseudocapacitive adsorption, especially for Zn^{2+}, which also leads to a greater specific capacitance. In Fig. 4b, the C_{sv} decreases as the scan rate increases since the rate of ion diffusion in solution can't keep up with the change of electrode potential [47]. The C_{sv} value of NSBc in the $ZnCl_2$ solution is 199 F g^{-1} at 5 mV s^{-1}, which is higher than that in the NaCl solution (172.6 F g^{-1}). In addition, it should be noted that the C_{sv} of NSBc is considerably increased compared to that of PBc, demonstrating the enhanced capacitance of NSBc, more specifically the
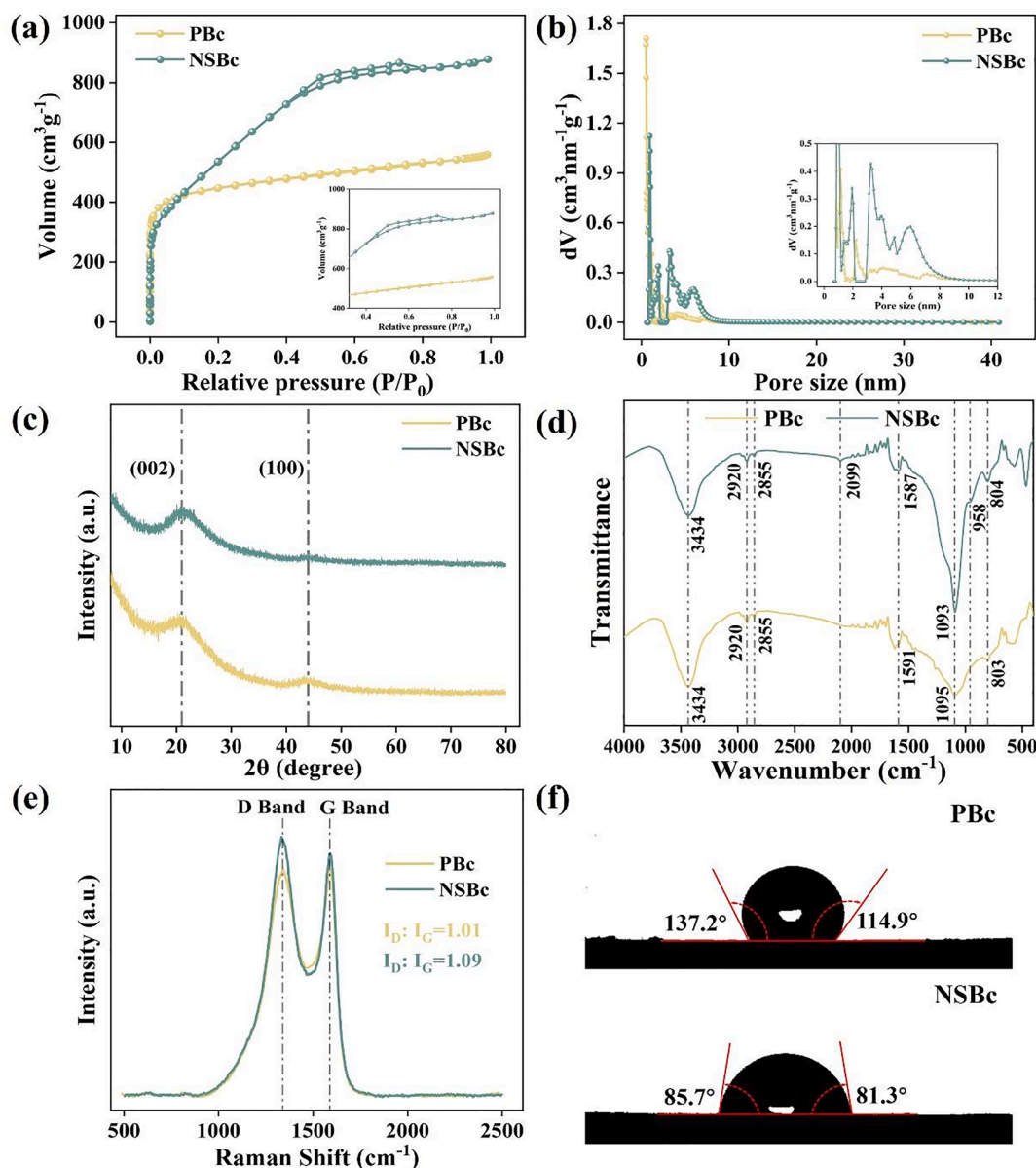
Fig. 3. (a) The N_2 adsorption/desorption isotherms; (b) The pore size distributions; (c) XRD patterns; (d) FT-IR spectra; (e) Raman spectra; (f) Water contact angle of PBc and NSBc.

remarkable Zn^{2+} adsorption capacity.

Fig. 4c displays the GCD curves of PBc and NSBc at a current density of 0.2 A g^{-1} in a NaCl or ZnCl$_2$ solution. NSBc exhibits an inverted triangle shape and the internal resistance drop of the discharge period is very small. At the potential range of $-0.6 - 0$ V, the electrode primarily adsorbs cations and the adsorption of Zn^{2+} is superior to that of Na$^+$ for NSBc, suggesting that it has a more favorable selectivity for Zn^{2+}. Furthermore, in comparison with PBc, the adsorption of Zn^{2+} by NSBc increases dramatically, implying that the doping of N, and S atoms elevates the electrochemical performance of the electrode. The C_s with various current densities for the electrodes is presented in Fig. 4d. The reduction of C_s with increasing current density is attributed to the concentration polarization resulting from the hindered ion diffusion under high current densities. More importantly, the C_s of NSBc in the ZnCl$_2$ solution (177.38 F g^{-1} at 0.2 A g^{-1}) is significantly higher than that of PBc (143.78 F g^{-1} at 0.2 A g^{-1}). Besides, compared with the NaCl solution (162.01 F g^{-1} at 0.2 A g^{-1}), NSBc exhibits larger C_s in the ZnCl$_2$ solution, which is conducive to the realization of selective Zn^{2+} adsorption. The doping of N, S atoms significantly raises the specific

surface area and new defects are created during the N atoms doping, which provides more active sites for ion adsorption [48,49]. The unique pore architecture of NSBc, characterized by interconnected micropores and mesopores as observed in the TEM results, likely shortens the ion diffusion distance and enhances ion transport from the bulk solution to the interface. Furthermore, the introduction of N and S atoms through doping brings about functional groups such as —SO$_3$H, which could potentially lead to a stronger electrostatic attraction for divalent Zn^{2+} compared to monovalent Na$^+$. Additionally, it is plausible that the pyridine N in NSBc has the capacity to specifically adsorb Zn^{2+}.

To further elucidate the ion transport process of NSBc in solutions containing Na$^+$ or Zn^{2+}, EIS analysis was employed to probe the charge transfer capability of the electrodes. As shown in Fig. 4e, the interfacial charge transfer resistance (R$_{ct}$) and the series resistance (R$_s$) including the contact resistance as well as the electrolyte resistance were determined by fitting the Nyquist plot. The slope of NSBc in ZnCl$_2$ solution is bigger than that in NaCl which corresponds to their smaller ion diffusion resistance and bigger capacitance [50]. Smaller R$_{ct}$ in ZnCl$_2$ (0.122 Ω) than in NaCl (0.359 Ω) reveals the outstanding interfacial charge
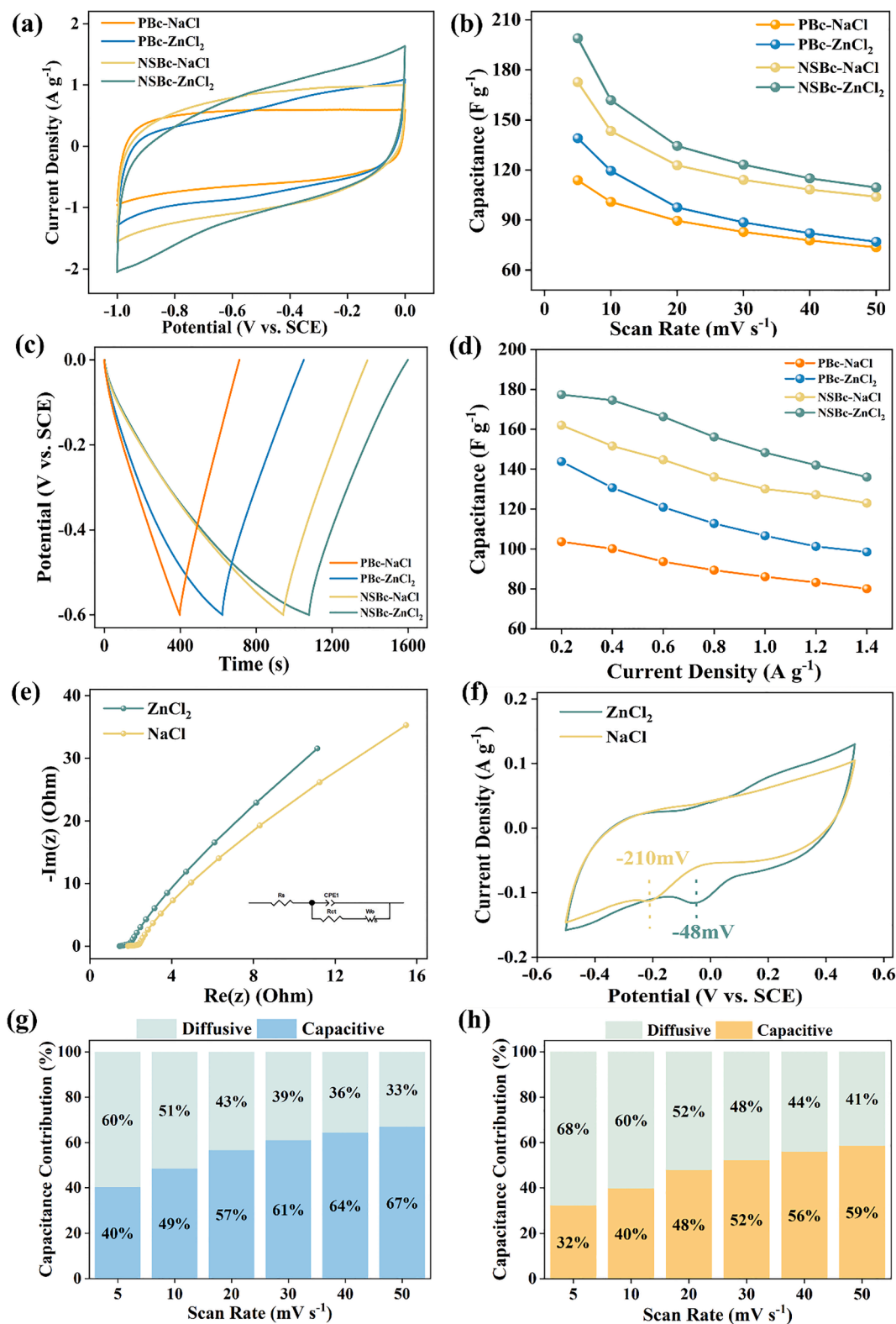
Fig. 4. Electrochemical tests. (a) CV curves of PBc and NSBc at 5 mV s^{-1}, (b) the specific capacitance at different scan rates, (c) GCD curves of PBc and NSBc at 0.2 A g^{-1}, (d) the specific capacitance at different current densities, (e) the Nyquist plots (the inset is the high-frequency region) of NSBc in different solutions, (f) Epzc of NSBc measured in a 5 mM solution at 1 mV^{-1}, capacitance contribution of NSBc in NaCl (g) and ZnCl$_2$ (h).

transfer ability of NSBc in ZnCl$_2$, which may be advantageous for selective Zn^{2+} removal [51,52]. After N, and S atoms doping, new functional groups are generated, and the changes of these functional groups to the electrode solid–liquid interface can substantially influence the CDI process. Epzc test was implemented to study the interface. As shown

in Fig. 4f, the Epzc of NSBc in both solutions is negative, suggesting that NSBc is positively charged with functional groups, which exclude cations from entering the pores. Interestingly, the Epzc value of NSBc in the ZnCl$_2$ solution is −48 mV while in the NaCl solution is −210 mV, which indicates that the co-ions effect of NSBc in the ZnCl$_2$ solution is

alleviated. This can be attributed to the stronger adsorption of Zn^{2+} by pyridine N, —SO_3H, and others; it further implies that NSBc is promising for Zn^{2+} removal.

To quantitatively compare the capacitance contribution of NSBc in NaCl and $ZnCl_2$, the CV data were processed mathematically for different scan rates. The ion adsorption process can be divided into capacitive controlled and diffusion controlled processes by Eq. (7) and Eq. (8):

$$i(V) = k_1 v + k_2 v^{1/2} \tag{7}$$

$$i(V)/v^{1/2} = k_1 v^{1/2} + k_2 \tag{8}$$

where $k_1 v$ and $k_2 v^{1/2}$ are the current densities of capacitive and diffusive processes, respectively [53]. The relationship of $i/v^{1/2}$ and $v^{1/2}$ for quantitative comparison of capacitance contributions is described in Fig. 4g and h. An increased capacitive contribution with increasing scanning rates was observed in both solutions, which was caused by the concentration polarization produced by the high scan rates. It is noteworthy that NSBc exhibits a larger diffusive contribution in the $ZnCl_2$ solution at any scan rate. This fully demonstrates the strong adsorption of Zn^{2+} by the functional group.

3.3. CDI performance

To verify the feasibility of N, S doping for efficient selective removal of Zn^{2+}, CDI experiments were carried out using a symmetric configuration in 1 mM $ZnCl_2$ solution at 1.0/0 V. During the CDI experiments, the results in NaCl solution were obtained by a conductivity meter, and the ion concentrations in the other solutions were obtained by ICP-OES analysis. As illustrated in Fig. 5a, the electrodes were firstly equilibrated in the CDI device with no voltage applied and the solution cycling. Both PBc and NSBc were observed to possess obvious physical adsorption of

Zn^{2+}. It is noteworthy that the initial adsorption capacity of 97.9 μmol g^{-1} for NSBc is much higher than that of 13.6 μmol g^{-1} for PBc, which is partly attributed to more adsorption sites from the increased specific surface area and defect ratio [44]. Moreover, it can be observed that NSBc has a more rapid Zn^{2+} adsorption rate, reaching 652.4 μmol g^{-1} SAC at 100 min, with an ASAR of 6.52 μmol g^{-1} min^{-1}, which is much higher than that of PBc (298.6 μmol g^{-1} and 2.99 μmol g^{-1} min^{-1}). The results in a single NaCl or $ZnCl_2$ solution are shown in Fig. 5b. NSBc exhibits superior adsorption capacity (274.4 μmol g^{-1} for Na^+, 652.4 μmol g^{-1} for Zn^{2+}), which was 3.1 and 2.2 times higher than that of PBc, respectively, indicating that NSBc has more active sites interacting with ions as an indicator of enhanced CDI performance. The results were further compared with reported results of Zn^{2+} adsorption in Table S1, showing excellent adsorption capacity and selectivity.

The competitive adsorption of Zn^{2+} towards Na^+ was conducted under a molar ratio of Zn^{2+}/Na^+ of 1:1 in Fig. 5c. The adsorption of Zn^{2+} by NSBc in the mixed solution reached 782.6 μmol g^{-1} with a selectivity coefficient β of 5.2 that is greater than that of PBc of 2.8, indicating an excellent Zn^{2+} selectivity of NSBc. The adsorption of Zn^{2+} in a mixed solution was higher than the value in a single $ZnCl_2$ solution, probably because the higher conductivity of the mixed solution favored the ion transport from the bulk solution to the interface. In Fig. 5d, NSBc achieved a β of 14.9 in a solution with a Na^+/Zn^{2+} molar ratio of 3:1, with the adsorption of Zn^{2+} of 706.4 μmol g^{-1}. The amount of adsorption was almost unchanged despite a further increase in the concentration of Na^+, suggesting that the NSBc provides stronger selective adsorption of Zn^{2+}.

In situ Raman was employed to reveal the role of the defects in the adsorption process. In Fig. 6a and b, NSBc has a higher percentage of defects than PBc, which is facilitated by the N doping altering the carbon skeleton, leading to extra adsorption sites. Moreover, no voltage was applied at 0 min and the electrode showed an initial physical adsorption. During the CDI process, it can be found that the defect ratio of NSBc decreases from 1.09 to 0.73, which is a higher drop than that of PBc
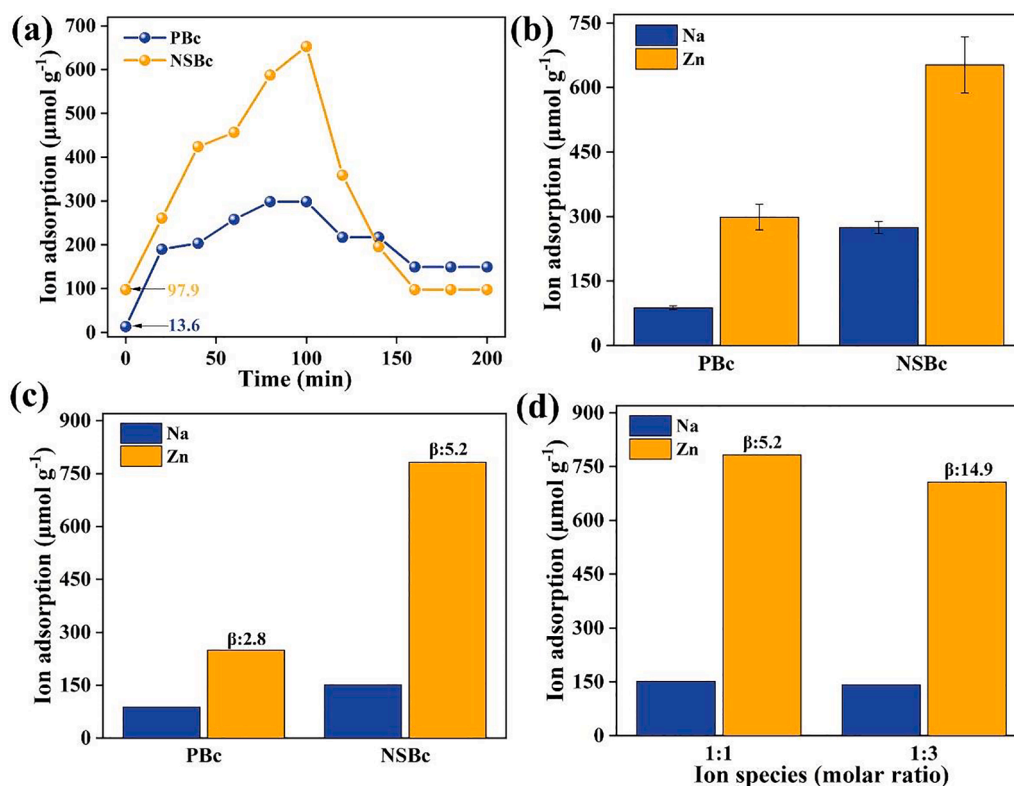

Fig. 5. (a) Zn^{2+} concentration variation of PBc and NSBc in 1 mM $ZnCl_2$ solution at 1.0/0 V, Adsorption capacity of Na^+/Zn^{2+} of PBc/NSBc (b) in a single NaCl or $ZnCl_2$ solution, (c) in multi-ion solution (molar ratios Na^+: Zn^{2+} = 1: 1), (d) Adsorption capacity of Na^+/Zn^{2+} of NSBc in mixed solution (molar ratio Na^+:Zn^{2+} = x: 1, x = 1, 3).
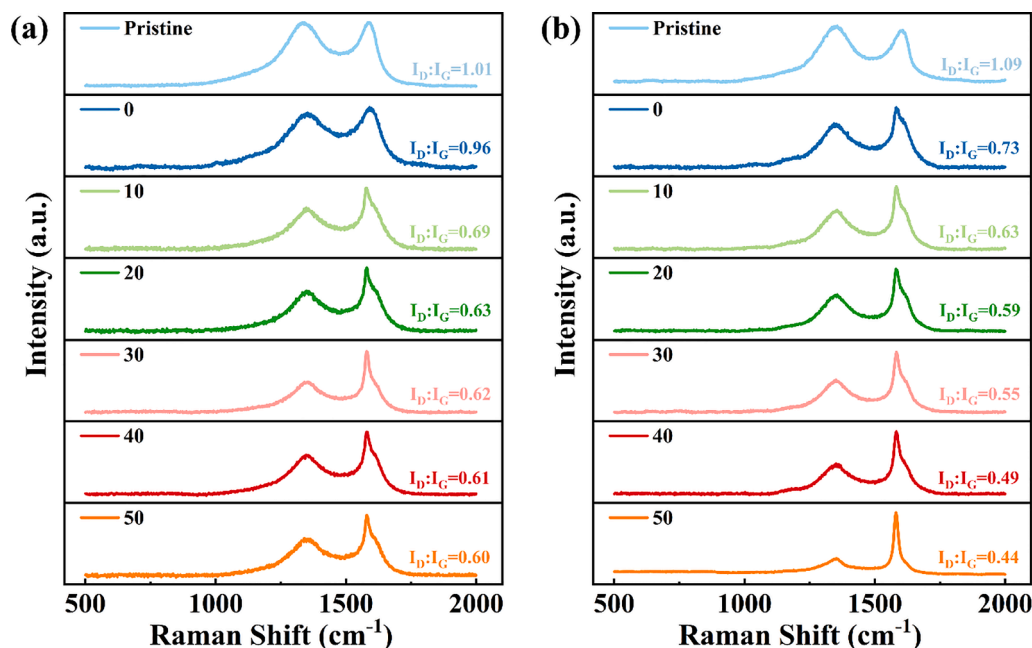
Fig. 6. In situ Raman of (a) PBc and (b) NSBc at 1.0 V in 1 mM NaCl and 1 mM ZnCl$_2$ mixed solution.

(from 1.01 to 0.96), which is consistent with the result obtained in the CDI experiments. The defects induced by N atoms doping in the carbon skeleton in NSBc, such as pyrrole N and pyridine N [54], have a strong adsorption effect on ions and thus show a higher degree of decrease. The defect ratio further drops as the time of applied voltage goes, indicating that the defects make a major contribution to the ion adsorption process. At the final stage, NSBc reaches a lower defect ratio (0.44) compared to PBc (0.60), which is explained by the fact that —SO$_3$H as well as pyridine N on the surface of the NSBc facilitated the ion adsorption. The in situ Raman indicates that the defects are significant for ion adsorption, and the doping of N, and S heavily enhances the adsorption capacity.

To elucidate the mechanism of Zn^{2+} adsorption, original NSBc as well as NSBc after use in a 1 mM ZnCl$_2$ solution at 1.0 V were further characterized by XPS. In Fig. 7a, the original NSBc surface was anchored with —SO$_3$H, favoring the adsorption of divalent Zn^{2+} compared to monovalent Na$^+$ by electrostatic forces [55]. Fig. 7b shows the fine spectra of Zn 2p with the peaks at 1021.8 and 1044.9 eV and the spin–orbit splitting of Zn 2p is 23.1 eV, which was consistent with the Zn^{2+} state [56]. In Fig. 7c and d, the O 1s fine spectra of NSBc before and after the experiment are demonstrated. The peak position of —OH shifted from 535.4 eV to 533.1 eV due to the substitution of the H atom of the —SO$_3$H or —COOH by Zn^{2+}. Zn^{2+} is less electronegative than H, leading to an increase in the density of the electron cloud around the O atom, which ultimately results in the decrease of the binding energy. Fig. 7e, f shows the N 1s fine spectra of NSBc before and after the CDI experiment. The presence of pyridine N and pyrrole N can promote surface-induced fast electrochemical kinetics, and graphite N can bring additional free electrons to improve the conductivity of the electrode [57]. Furthermore, the binding energy position of pyridine N increased from 397.4 eV to 399.4 eV, which implies that Zn^{2+} was adsorbed to the pyridine N site to form a new chemical bond, and the transfer of the lone pair electrons from pyridine nitrogen to Zn^{2+} led to a decrease in the density of the electron cloud. The above analyses demonstrated that NSBc has a unique adsorption capacity for Zn^{2+} and has a broad application prospect in the selective removal of Zn^{2+}.

3.4. Theoretical validation

To validate the selective adsorption of Zn^{2+} over Na$^+$, density functional theory (DFT) calculations were performed for NaCl and ZnCl$_2$

when positioned above graphite slabs with N or S dopants. Given the uncertainty in the locations of the N or S dopants in the experimental setup, three adsorption modes—basal plane, zigzag edge, and armchair edge—were considered. For the basal plane mode, the slab has three layers of ABA stacking with 3.414 Å inter-layer separation along the z-direction and 2.462 Å intra-layer lattice constant along the xy-plane (Fig. 8a). Each layer in the slab is extended along the xy-plane and has 32 C atoms (96 in total). To eliminate the spurious self-interaction between the slabs along the z-direction, a 20 Å vacuum is introduced along this axis. Next, two unique doped slabs are created by replacing one of the C atoms in the topmost surface with N or S. NaCl or ZnCl$_2$ are added (slab + molecule system) parallel to the basal plane such that the metal site (Na/Zn) lies directly above N or S. The initial separation between the metal site and the N atom is 2 Å while the separation of the metal site with the S atom is 3.5 Å (Fig. S1). Four systems were evaluated in total. A similar procedure was adopted for zigzag and armchair edge modes (Figs. S2 and S3). We note here that during the construction of the slab for armchair and zigzag modes, hydrogen atoms were bonded to the C atoms lying on the edge surface to balance the charges (Figs. S2 and S3).

Our motivation behind modeling the adsorption of NaCl and ZnCl$_2$ in an aqueous solution (as an implicit solvent) is to mimic the experimental setup that focuses on the adsorption strength of Na$^+$ and Zn^{2+} so that we could make a direct comparison between our results and the findings from the experiment. Throughout the text, we will be referring to the adsorption energies associated with NaCl and ZnCl$_2$ as those of Na$^+$ and Zn^{2+}. Our setup captures the interaction of charged metallic ions and the slab implicitly; this was a choice we made to avoid the calculation of charged systems with DFT. Fig. 8b displays the general trends of adsorption energy of NaCl and ZnCl$_2$ across N- and S-doped slabs (see Table S2 in the supplementary materials for exact numbers). With approximately three times greater adhesion (0.23 eV vs 0.98 eV for N-doped slab, and 0.44 eV vs 1.16 eV for S-doped slab), it is seen that the strength of Zn^{2+} adsorption notably surpasses that of Na$^+$. This indicates the superior selective adsorption capacity of Zn^{2+} over Na$^+$. Fig. 8b also suggests a heightened adsorption tendency for both Na$^+$ and Zn^{2+} with the introduction of defects and functional groups, particularly S-doping enhancing the adsorption process. These observations support the experimental findings that there is an augmentation in the electrosorption facilitated by element doping.

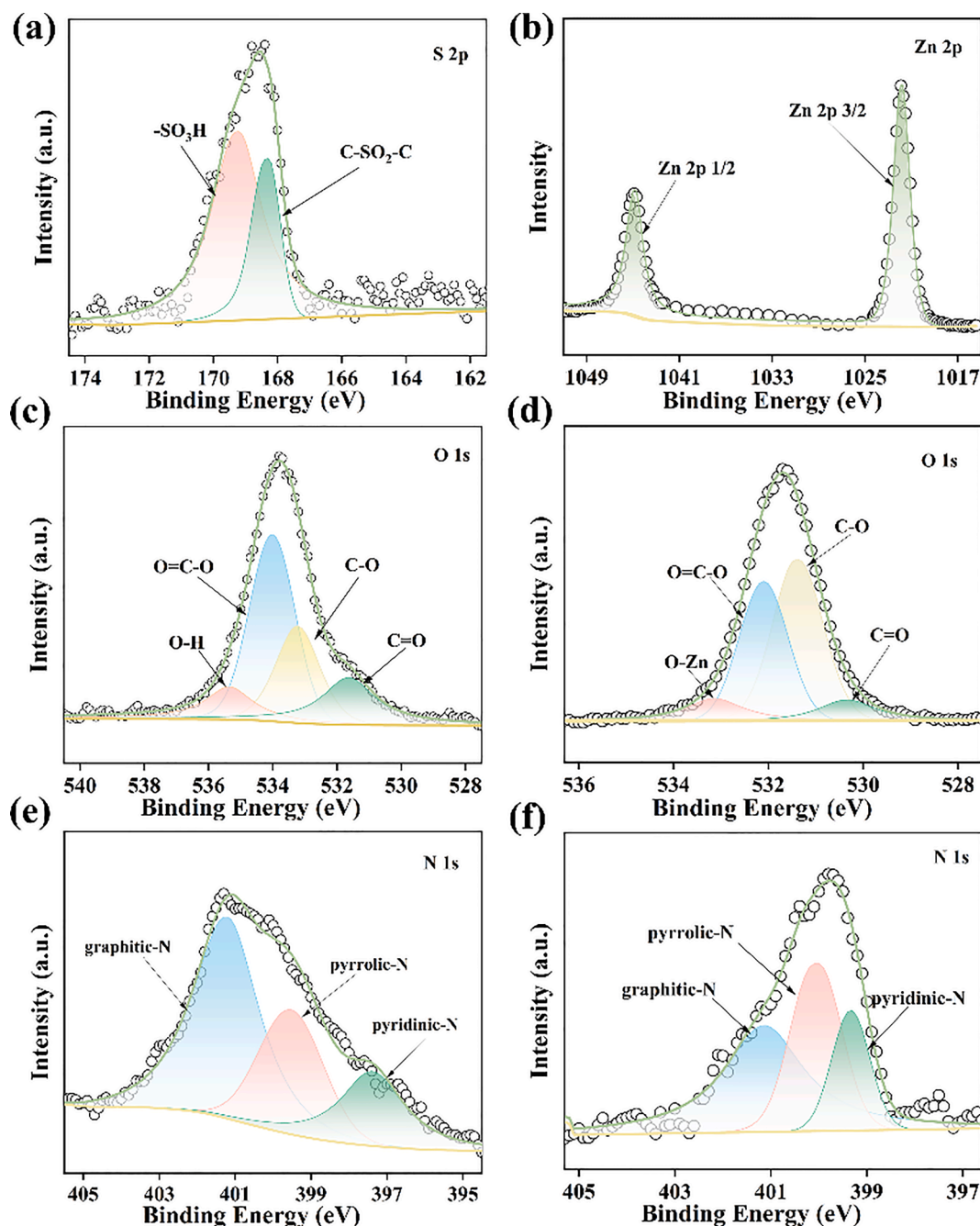To further understand the mechanisms for enhanced adsorption, we

Fig. 7. XPS spectra of (a) S 2p for original NSBc electrode; (b) Zn 2p after testing in 1 mM ZnCl$_2$; (c), (d) O 1s before and after testing in 1 mM ZnCl$_2$; (e), (f) N 1s before and after testing in 1 mM ZnCl$_2$.

investigated the impact of charge transfer between the metal site (Na/Zn) and the slab on the observed adsorption energies. We analyze the net atomic charges obtained from the recently introduced density-derived electrostatic and chemical 6 (DDEC6) method [58,59] which has been demonstrated to have the capability to reliably partition the charges [60,61]. The nature and the magnitude of the net charges exchanged between NaCl/ZnCl$_2$ and the slab (see column Δq, Table S2) support the observed trends of adsorption. Particularly, ZnCl$_2$ (compared to NaCl) displays a significant bonding charge transfer with N/S and other nearby C atoms lying on the top surface, representing stronger adsorption strength. This observation aligns well with our EIS analysis that the interfacial charge transfer ability of NSBc in ZnCl$_2$ is superior to that in NaCl. Furthermore, the increased charge density around the Zn site (as indicated by net negative bonding charges in Table S2) indicates a

significant covalent bonding between the slab and Zn [58]. On the other hand, NaCl (compared to ZnCl$_2$) exhibits negligible bonding charge transfer indicating a weaker interaction with the slab as displayed in Fig. 8c.

4. Conclusion

The N, S doped hierarchical porous carbon with a large ion-accessible surface area was prepared for selective Zn^{2+} removal from low-concentration Zn-containing wastewater. NSBc shows a sponge-like structure with macropore, mesopore, and micropore distributed in the material to provide an excellent pore structure for ion adsorption. The electrode achieved 706.4 μmol g^{-1} of Zn^{2+} adsorption at 1.0 V and a selectivity factor of 14.9 in a mixed solution of Zn^{2+} and Na$^+$ with a ratio
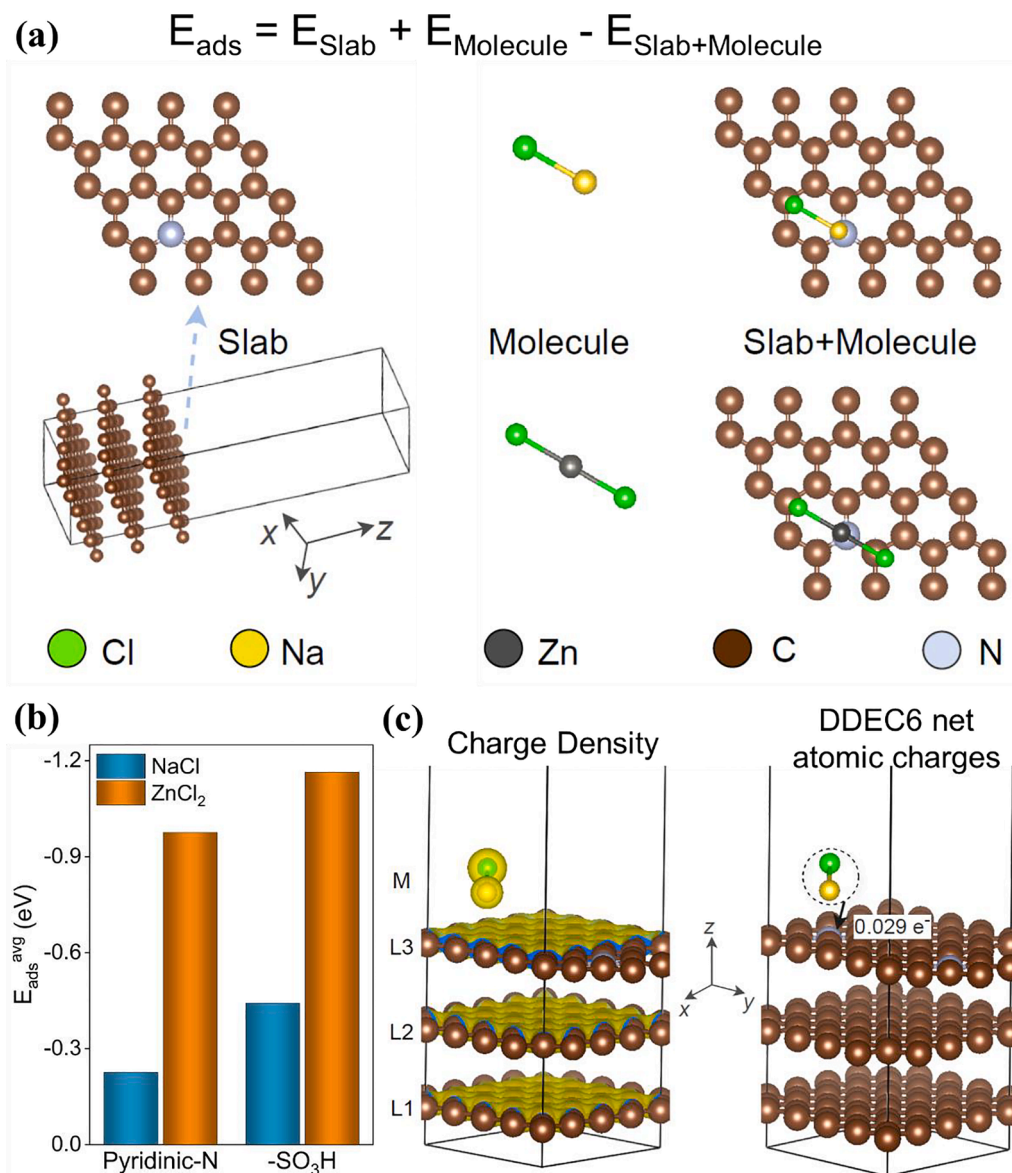
Fig. 8. (a)Schematic overview of the slab-molecule heterostructure construction (N-doped Basal plane) for adsorption energy calculations (S-doped case in Fig. S1 for details). (b) Comparison of average adsorption energies of NaCl and ZnCl$_2$ over the N- and S- doped site in graphite in an aqueous solution. (c) The charge density distribution and the net bonding charge transfer in the NaCl slab system. L1, L2, L3, and M represent the position along the z-axis of the bottom, middle, the topmost layers of the slab and NaCl, respectively. The black solid arrow in the right panel indicates 0.029 e$^-$ charge transferred from NaCl to the slab.

of 1:3. The NSBc maintained excellent Zn^{2+} adsorption under different conditions, which sufficiently proved the feasibility of the strategy. Moreover, in situ Raman technique profoundly elaborated that the defects created by N doping were favorable to promoting Zn^{2+} adsorption. XPS technique revealed that the existence of specific adsorption of Zn^{2+} by N, S functional groups including pyridine N, —SO$_3$H was favorable to improve the selectivity of biochar in the Zn^{2+} mixed solution. DFT calculations supported the experimental findings that the N, S doping enhanced the adsorption strength of Zn^{2+}. We believe that this work can provide a fresh perspective on the application of CDI technology for the treatment of industrial wastewater containing low concentrations of Zn^{2+}.

CRediT authorship contribution statement

Changlin Wang: Conceptualization, Methodology, Investigation, Writing – original draft. **Santosh Adhikari:** Methodology, Investigation, Writing – original draft. **Yuqi Li:** Investigation, Writing – review &

editing. **Mingjian Wen:** Writing – review & editing, Supervision. **Yang Wang:** Conceptualization, Methodology, Writing – review & editing, Supervision, Funding acquisition.

Declaration of competing interest

The authors declare that they have no known competing financial interests or personal relationships that could have appeared to influence the work reported in this paper.

Data availability

Data will be made available on request.

Appendix A. Supplementary data

Supplementary data to this article can be found online at https://doi.org/10.1016/j.seppur.2024.129446.

References

[1] L. Chen, G. Zhang, H. Liu, S. Miao, Q. Chen, H. Lan, J. Qu, Efficient metal recovery from industrial wastewater: potential oscillation and turbulence mode for electrochemical system, Engineering (2024).

[2] Y. Zhou, J. Xia, J. Di, Z. Sun, L. Zhao, L. Li, Y. Wu, L. Dong, X. Wang, Q. Li, Ultrahigh-rate Zn stripping and plating by capacitive charge carriers enrichment boosting Zn-based energy storage, Adv. Energy Mater. 13 (2023) 2203165.

[3] S.L. Huang, C.-Y. Yin, S.Y. Yap, Particle size and metals concentrations of dust from a paint manufacturing plant, J. Hazard. Mater. 174 (2010) 839–842.

[4] R. Petrus, P. Sobota, Magnesium and zinc alkoxides and aryloxides supported by commercially available ligands as promoters of chemical transformations of lactic acid derivatives to industrially important fine chemicals, Coord. Chem. Rev. 396 (2019) 72–88.

[5] W.-P. Zhu, S.-P. Sun, J. Gao, F.-J. Fu, T.-S. Chung, Dual-layer polybenzimidazole/polyethersulfone (PBI/PES) nanofiltration (NF) hollow fiber membranes for heavy metals removal from wastewater, J. Membr. Sci. 456 (2014) 117–127.

[6] A.H. Jagaba, S.R.M. Kutty, S.G. Khaw, C.L. Lai, M.H. Isa, L. Baloo, I.M. Lawal, S. Abubakar, I. Umaru, Z.U. Zango, Derived hybrid biosorbent for zinc(II) removal from aqueous solution by continuous-flow activated sludge system, J. Water Process Eng. 34 (2020) 101152.

[7] E.D.d. Freitas, H.J.d. Almeida, M.G.A. Vieira, Binary adsorption of zinc and copper on expanded vermiculite using a fixed bed column, Appl. Clay Sci. 146 (2017) 503–509.

[8] S. Hussain, M. Khan, T.M.M. Sheikh, M.Z. Mumtaz, T.A. Chohan, S. Shamim, Y. Liu, Zinc essentiality, toxicity, and its bacterial bioremediation: a comprehensive insight, Front. Microbiol. 13 (2022).

[9] Z.T. Alismaeel, A.H. Abbar, O.F. Saeed, Application of central composite design approach for optimisation of zinc removal from aqueous solution using a Flow-by fixed bed bioelectrochemical reactor, Sep. Purif. Technol. 287 (2022) 120510.

[10] A. Jakobik-Kolon, J. Bok-Badura, K. Karon, K. Mitko, A. Milewski, Hybrid pectin-based biosorbents for zinc ions removal, Carbohydr. Polym. 169 (2017) 213–219.

[11] B. Li, H. Huang, Z. Sun, N. Zhao, T. Munir, W. Yu, B. Young, Minimizing heavy metals in recovered struvite from swine wastewater after anaerobic biochemical treatment: reaction mechanisms and pilot test, J. Clean. Prod. 272 (2020) 122649.

[12] Y. Liu, X. Ke, H. Zhu, R. Chen, X. Chen, X. Zheng, Y. Jin, B. Van der Bruggen, Treatment of raffinate generated via copper ore hydrometallurgical processing using a bipolar membrane electrodialysis system, Chem. Eng. J. 382 (2020) 122956.

[13] X. Ren, Q. Wei, S. Hu, S. Wei, The recovery of zinc from hot galvanizing slag in an anion-exchange membrane electrolysis reactor, J. Hazard. Mater. 181 (2010) 908–915.

[14] F. Fu, Q. Wang, Removal of heavy metal ions from wastewaters: a review, J. Environ. Manage. 92 (2011) 407–418.

[15] S.S. Lim, J.M. Fontmorin, E. Milner, P.M. Abdul, K. Scott, I. Head, E.H. Yu, Zinc removal and recovery from industrial wastewater with a microbial fuel cell: experimental investigation and theoretical prediction, Sci. Total Environ. 776 (2021) 145934.

[16] S. Ntakirutimana, W. Tan, M.A. Anderson, Y. Wang, Editors' choice—review—activated carbon electrode design: engineering tradeoff with respect to capacitive deionization performance, J. Electrochem. Soc. 167 (2020) 143501.

[17] K. Sun, M. Tebyetekerwa, C. Wang, X. Wang, X. Zhang, X.S. Zhao, Electrocapacitive deionization: mechanisms, electrodes, and cell designs, Adv. Funct. Mater. 33 (2023) 2213578.

[18] D. Deng, B. Chen, C. Zhao, M.A. Anderson, Y. Wang, Importance of anode/cathode mass loadings on capacitive deionization performance, J. Electrochem. Soc. 168 (2021) 053503.

[19] Q. Li, Y. Zheng, D. Xiao, T. Or, R. Gao, Z. Li, M. Feng, L. Shui, G. Zhou, X. Wang, Z. Chen, Faradaic electrodes open a new era for capacitive deionization, Adv. Sci. 7 (2020) 2002213.

[20] M.S. Gaikwad, C. Balomajumder, A.K. Tiwari, Acid treated RHWBAC electrode performance for Cr(VI) removal by capacitive deionization and CFD analysis study, Chemosphere 254 (2020) 126781.

[21] N. Wang, M. Wang, H. Quan, S. Wang, D. Chen, Waste Camellia oleifera shell-derived hierarchically porous carbon modified by Fe3O4 nanoparticles for capacitive removal of heavy metal ions, Sep. Purif. Technol. 329 (2024) 125184.

[22] H. Huang, Y. Chen, R. Ma, J. Luo, S. Sun, J. Lin, Y. Wang, Preparation of high performance porous carbon by microwave synergistic nitrogen/phosphorus doping for efficient removal of Cu2+ via capacitive deionization, Environ. Res. 222 (2023) 115342.

[23] D. Deng, M.K. Luhasile, H. Li, Q. Pan, F. Zheng, Y. Wang, A novel layered activated carbon with rapid ion transport through chemical activation of chestnut inner shell for capacitive deionization, Desalination 531 (2022) 115685.

[24] Y. Li, C. Wang, D. Deng, Y. Qiao, G. Yao, Y. Wang, Asymmetric capacitive deionization based on pore structures of biochar, Desalination 583 (2024) 117675.

[25] C. Wang, Y. Li, Y. Qiao, N.L. Tut, D. Deng, Q. Pan, G. Yao, Y. Wang, The regulation of biochar surface potential to achieve rapid capacitive deionization, J. Environ. Chem. Eng. 11 (2023) 111560.

[26] G. Kresse, J. Furthmüller, Efficiency of ab-initio total energy calculations for metals and semiconductors using a plane-wave basis set, Comput. Mater. Sci 6 (1996) 15–50.

[27] G.a.F.u.J. Kresse, Efficient iterative schemes for ab initio total-energy calculations using a plane-wave basis set, Phys. Rev. B 54 (1996) 11169–11186.

[28] P.E. Blöchl, Projector augmented-wave method, PhRvB 50 (1994) 17953–17979.

[29] G. Kresse, D. Joubert, From ultrasoft pseudopotentials to the projector augmented-wave method, PhRvB 59 (1999) 1758–1775.

[30] J.P.a.B. Perdew, Kieron, Ernzerhof, Matthias, Generalized Gradient Approximation Made Simple, Phys. Rev. Lett. 77 (1996) 3865–3868.

[31] A. Tkatchenko, R.A. DiStasio, R. Car, M. Scheffler, Accurate and efficient method for many-body van der Waals interactions, Phys. Rev. Lett. 108 (2012) 236402.

[32] R. Wu, L. Wang, Insight into the solvent effects on ethanol oxidation on Ir(100), PCCP 25 (2023) 2190–2202.

[33] M. Long, J. Donoso, M. Bhati, W.C. Elias, K.N. Heck, Y.-H. Luo, Y.S. Lai, H. Gu, T.P. Senftle, C. Zhou, M.S. Wong, B.E. Rittmann, Adsorption and reductive defluorination of perfluorooctanoic acid over palladium nanoparticles, Environ. Sci. Tech. 55 (2021) 14836–14843.

[34] K. Mathew, R. Sundararaman, K. Letchworth-Weaver, T.A. Arias, R.G. Hennig, Implicit solvation model for density-functional study of nanocrystal surfaces and reaction pathways, J. Chem. Phys. 140 (2014) 084106.

[35] K. Mathew, V.S.C. Kolluru, S. Mula, S.N. Steinmann, R.G. Hennig, Implicit self-consistent electrolyte model in plane-wave density-functional theory, J. Chem. Phys. 151 (2019) 234101.

[36] S. Wu, P. Yan, W. Yang, J. Zhou, H. Wang, L. Che, P. Zhu, ZnCl2 enabled synthesis of activated carbons from ion-exchange resin for efficient removal of Cu2+ ions from water via capacitive deionization, Chemosphere 264 (2021) 128557.

[37] T. Gao, Y. Du, H. Li, Preparation of nitrogen-doped graphitic porous carbon towards capacitive deionization with high adsorption capacity and rate capability, Sep. Purif. Technol. 211 (2019) 233–241.

[38] H. Zhang, J. Tian, X. Cui, J. Li, Z. Zhu, Highly mesoporous carbon nanofiber electrodes with ultrahigh specific surface area for efficient capacitive deionization, Carbon 201 (2023) 920–929.

[39] W. Bao, X. Tang, X. Guo, S. Choi, C. Wang, Y. Gogotsi, G. Wang, Porous cryo-dried MXene for efficient capacitive deionization, Joule 2 (2018) 778–787.

[40] G.-X. Li, P.-X. Hou, S.-Y. Zhao, C. Liu, H.-M. Cheng, A flexible cotton-derived carbon sponge for high-performance capacitive deionization, Carbon 101 (2016) 1–8.

[41] X. Min, X. Hu, X. Li, H. Wang, W. Yang, Synergistic effect of nitrogen, sulfur-codoping on porous carbon nanosheets as highly efficient electrodes for capacitive deionization, J. Colloid Interface Sci. 550 (2019) 147–158.

[42] A. Levent, C. Saka, Enhanced electrochemical performance of ZnO@sulphur-doped carbon particles for use in supercapacitors, J. Storage Mater. 78 (2024) 110120.

[43] C. Saka, Sulphur and nitrogen-doped metal-free microalgal carbon catalysts for very active dehydrogenation of sodium borohydride in methanol, Int. J. Hydrogen Energy 46 (2021) 18326–18337.

[44] Y. Xu, Y. Gao, S. Xiang, J. Zhou, F. Liu, Z. Li, H. Zhou, Selective pseudocapacitive separation of zinc ions via silk cocoon derived N-doped porous carbon, Desalination 546 (2023) 116220.

[45] S.-M. Zheng, Z.-H. Yuan, D.D. Dionysiou, L.-B. Zhong, F. Zhao, J.-C.-E. Yang, Y.-M. Zheng, Silkworm cocoon waste-derived nitrogen-doped hierarchical porous carbon as robust electrode materials for efficient capacitive desalination, Chem. Eng. J. 458 (2023) 141471.

[46] A. Yousef, R.M. Abdel Hameed, S.F. Shaikh, A. Abutaleb, M.M. El-Halwany, A.M. Al-Enizi, Enhanced electro-adsorption desalination performance of graphene by TiC, Sep. Purif. Technol. 254 (2021) 117602.

[47] Z. Zhang, Y. Zhang, C. Jiang, D. Li, Z. Zhang, K. Wang, W. Liu, X. Jiang, Y. Rao, C. Xu, X. Chen, N. Meng, Highly efficient capacitive desalination for brackish water using super activated carbon with ultra-high pore volume, Desalination 529 (2022) 115653.

[48] P. Nie, X. Shang, B. Hu, T. Hussain, J. Yang, M. Huang, J. Liu, Enhanced capacitive removal of hardness ions by hierarchical porous carbon cathode with high mesoporosity and negative surface charges, J. Colloid Interface Sci. 612 (2022) 277–286.

[49] X. Gong, S. Feng, L. Wang, D. Jia, N. Guo, M. Xu, L. Ai, Q. Ma, Q. Zhang, Z. Wang, Defect-rich hierarchical porous carbon prepared by homogeneous activation for high performance capacitive deionization, Desalination 564 (2023) 116766.

[50] B. Zhang, Q. Liu, K. Xu, R. Zou, C. Wang, Electrochemical energy storage application of CuO/CuO@Ni–CoMoO4·0.75H2O nanobelt arrays grown directly on Cu foam, Prog. Nat. Sci.: Mater. Int. 32 (2022) 163–170.

[51] S. Huo, W. Ni, X. Song, M. Zhang, H. Wang, K. Li, Insight from the synergistic effect of dopant and defect interplay in carbons for high-performance capacitive deionization, Sep. Purif. Technol. 281 (2022) 119807.

[52] P.-I. Liu, L.-C. Chung, C.-H. Ho, H. Shao, T.-M. Liang, M.-C. Chang, C.-C.-M. Ma, R.-Y. Horng, Comparative insight into the capacitive deionization behavior of the

activated carbon electrodes by two electrochemical techniques, Desalination 379 (2016) 34–41.

[53] Z. Bo, X. Lu, H. Yang, S. Wu, X. Cheng, B. Gong, Z. Huang, J. Yan, K. Cen, K. Ostrikov, Surface-dominant pseudocapacitive supercapacitors with high specific energy and power for energy storage, J. Storage Mater. 42 (2021) 103084.

[54] F. Meng, Y. Liu, Z. Ding, L. Xu, H. Wang, X. Xu, X. Liu, T. Lu, L. Pan, Hydrogen-bonded organic framework derived 2D N, O Co-doped carbon nanobelt with tunable pseudocapacitive contribution for efficient capacitive deionization, Small 20 (2024) e2309353.

[55] R.L. Zornitta, F.J. García-Mateos, J.J. Lado, J. Rodríguez-Mirasol, T. Cordero, P. Hammer, L.A.M. Ruotolo, High-performance activated carbon from polyaniline for capacitive deionization, Carbon 123 (2017) 318–333.

[56] S.-M. Zheng, B. Li, Z.-H. Yuan, J.-C.-E. Yang, J. Zhang, L.-B. Zhong, Y.-M. Zheng, Zinc oxide nanosheet decorated self-supporting hierarchical porous wood carbon electrode for efficient capacitive deionization defluorination, Sep. Purif. Technol. 317 (2023) 123830.

[57] D. Zhang, H. Zhang, F. Gao, G. Huang, Z. Shang, C. Gao, X. Chen, J. Wei, M. Terrones, Y. Wang, Dual activation for tuning N, S co-doping in porous carbon sheets toward superior sodium ion storage, Small 20 (2024) 2308684.

[58] N.G. Limas, T.A. Manz, Introducing DDEC6 atomic population analysis: part 2. Computed results for a wide range of periodic and nonperiodic materials, RSC Adv. 6 (2016) 45727–45747.

[59] T.A. Manz, N.G. Limas, Introducing DDEC6 atomic population analysis: part 1. Charge partitioning theory and methodology, RSC Adv. 6 (2016) 47771–47801.

[60] M. Wells, J. Hempel, S. Adhikari, Q. Wang, D. Allen, A. Costello, C. Bowen, S. Parkin, C. Sutton, A.J. Huckaba, Structure and piezoelectricity due to B site cation variation in ABn+Cln+2 hybrid Histammonium Chlorometallate materials, Inorg. Chem. 61 (2022) 17746–17758.

[61] W. Sun, C.J. Bartel, E. Arca, S.R. Bauers, B. Matthews, B. Orvañanos, B.-R. Chen, M. F. Toney, L.T. Schelhas, W. Tumas, J. Tate, A. Zakutayev, S. Lany, A.M. Holder, G. Ceder, A map of the inorganic ternary metal nitrides, Nat. Mater. 18 (2019) 732–739.